Non-stationary teleconnection between the Pacific Ocean and Arctic sea ice

D.B. Bonan[1] and E. Blanchard-Wrigglesworth[2]

[1]Environmental Science and Engineering, California Institute of Technology, Pasadena, CA, USA
[2]Department of Atmospheric Sciences, University of Washington, Seattle, WA, USA

Key Points:

- An observed teleconnection between Pacific Ocean SSTs and Arctic sea-ice extent is analyzed in 30 fully-coupled GCMs participating in CMIP5
- Summer SST anomalies in the Pacific Ocean modulate September Arctic sea ice loss through changes in upper Arctic air conditions
- This teleconnection is found to be non-stationary on multidecadal timescales both in the GCMs able to simulate it and in observations

Corresponding author: David B. Bonan, `dbonan@caltech.edu`

Abstract

Over the last 40 years observations show a teleconnection between summertime Pacific Ocean sea-surface temperatures and September Arctic sea-ice extent. However, the short satellite observation record has made it difficult to further examine this relationship. Here, we use 30 fully-coupled general circulation models (GCMs) participating in Phase 5 of the Coupled Model Inter-comparison Project to assess the ability of GCMs to simulate this teleconnection and analyze its stationarity over longer timescales. GCMs can temporarily simulate the teleconnection in continuous 40-year segments, but not over longer, centennial timescales. Each GCM exhibits considerable teleconnection variability on multidecadal timescales. Further analysis shows the teleconnection depends on an equally non-stationary atmospheric bridge from the subequatorial Pacific Ocean to the upper Arctic troposphere. These findings indicate the modulation of Arctic sea ice loss by subequatorial Pacific Ocean variability is not fixed in time, undermining the assumption of teleconnection stationarity as defined by the satellite record.

Plain Language Summary

Understanding the processes leading to Arctic sea ice change remains a central goal in climate science. These changes affect not only weather and climate, but also local ecosystems, indigenous populations, and socio-economic activities in the region. Recent studies have shown that during the summer months, the Pacific Ocean influences Arctic sea ice. Such a relationship suggests that this region of the Pacific Ocean may be a key source of predictability for Arctic sea ice, especially for the summer minimum. However, our understanding of this relationship is derived from a short observational record, which makes it difficult to study how this relationship evolves over time. To overcome this limitation, we use long simulations from 30 different global climate models. We show that models are able to simulate this relationship, but the relationship changes considerably over time. This suggests the observed link between the Pacific Ocean and Arctic sea ice may change in the coming decades; therefore, caution should be applied when forecasting or reconstructing Arctic sea ice and assuming that this relationship is constant in time.

1 Introduction

Sea ice is a major component of the Arctic environment. It shapes the local ecosystems (Wyllie-Echeverria & Wooster, 1998), the life of indigenous populations (Ford & Smit, 2004), and the level of socio-economic activities in the region (Pizzolato et al., 2016; Melia et al., 2016). Over the last few decades, satellite observations have revealed that Arctic sea ice has undergone striking changes, a significant fraction of which is attributed to anthropogenic climate change (e.g., Kay et al., 2011; Ding et al., 2019). There has been a sharp decline in sea-ice extent, especially in summer and fall (Stroeve et al., 2007; Serreze et al., 2007; Comiso et al., 2008; Serreze & Meier, 2018), substantial thinning across all months (Rothrock et al., 1999; Kwok & Rothrock, 2009), and a notable loss of multiyear ice (Johannessen et al., 1999; Rigor & Wallace, 2004; Maslanik et al., 2011). Given the importance of Arctic sea ice, these changes have motivated a widespread effort to better understand the predictability of Arctic sea ice (e.g., Eicken, 2013; Jung et al., 2016).

A quantitative picture of Arctic sea-ice predictability is beginning to emerge. Studies on potential predictability in fully-coupled general circulation models (GCMs; e.g., Holland et al., 2011; Blanchard-Wrigglesworth, Bitz, & Holland, 2011; Day, Tietsche, & Hawkins, 2014; Tietsche et al., 2014; Bushuk et al., 2019) and statistical and dynamical forecast systems (e.g., W. Wang et al., 2013; Merryfield et al., 2013; Sigmond et al., 2013; Chevallier et al., 2013; Msadek et al., 2014; Blanchard-Wrigglesworth et al., 2015; Guemas et al., 2016; L. Wang et al., 2016; Petty et al., 2017; Bushuk et al., 2017) have shown that forecasts of pan-Arctic sea-ice extent (SIE) may be skillful anywhere between 2 months and 2 years in advance. At regional scales — which is often more societally relevant — dynamical prediction systems can skillfully predict SIE on seasonal timescales (Bushuk et al., 2017) or even decadal timescales (Yeager et al., 2015). While these results are certainly promising, more recent work has shown that prediction skill for regional summer SIE drops significantly for forecasts initialized prior to May (Bushuk et al., 2017, 2019), possibly limiting accurate summer forecasts for stakeholders. The existence of this "spring predictability barrier" is also found to be remarkably robust across dynamical models, with all GCMs participating in phase 5 of the Coupled Model Intercomparison Project (CMIP5) displaying a predictability barrier structure in late spring (Bonan, Bushuk, & Winton, 2019). This barrier, along with mounting evidence for a significant gap between the potential and operational forecast skill of Arctic SIE (Blanchard-Wrigglesworth et al., 2015; Bushuk et al., 2019) and the possibility that GCMs may overestimate sea-ice predictability (Blanchard-Wrigglesworth & Bushuk, 2019), motivates the need to better understand physically-based mechanisms for Arctic sea-ice predictability. An improved understanding may improve operational forecasts.

For summer Arctic sea ice, in particular, considerable effort has gone toward identifying such mechanisms. Numerous variables have been found to offer information on prediction skill, including: sea-ice thickness (Blanchard-Wrigglesworth, Armour, et al., 2011; Day, Hawkins, & Tietsche, 2014; Dirkson et al., 2017; Bushuk et al., 2017; Bonan, Bushuk, & Winton, 2019), sea-ice motion in the winter (Williams et al., 2016), melt pond fraction in the spring (Schröder et al., 2014), ocean heat fluxes (Woodgate et al., 2010), stratospheric conditions (Smith et al., 2018), longwave radiation in the spring (Kapsch et al., 2013), surface winds (Ogi et al., 2010), and tropospheric temperatures in the summer (Ding et al., 2017). Remote processes have also been found to impact summer Arctic sea ice. Summer tropical Pacific sea surface temperatures (SSTs), for instance, modulate interannual changes in the Arctic environment via atmospheric wave propagation (Ding et al., 2014; Hu et al., 2016; Ding et al., 2019; Baxter et al., 2019). The preferred circulation response or "atmospheric teleconnection" to a particular SST pattern results from a large-scale barotropic Rossby wave train that causes interactions between the mean flow anomaly and transient eddies (see review by Trenberth et al., 1998). Throughout the year, numerous atmospheric teleconnections can influence Arctic sea ice (L'Heureux et al., 2008; Screen & Francis, 2016; Meehl et al., 2018; Ding et al., 2019; Screen & Deser, 2019; Baxter et al., 2019; Castruccio et al., 2019). For example, Baxter et al. (2019) show that cool SST anomalies in the subequatorial Pacific Ocean leads to reduced local convection, which generates anomalous upper level divergence that, in turn, creates a barotropic Rossby wave train propagation from the tropical Pacific Ocean to the Arctic. Referred to as the "Pacific-Arctic (PARC) teleconnection", this wave train favors persistent positive geopotential height anomalies centered over northeastern Canada and Greenland. Positive geopotential height anomalies cause large scale subsidence in the Arctic that adiabatically warms the atmosphere above the sea ice, which increases downward longwave radiation and leads to increases in sea ice melt (Ding et al., 2019). Since it is thought the PARC teleconnection has contributed to accelerated Arctic sea ice loss in recent years (Baxter et al., 2019), it is crucial to quantify the ability of GCMs to correctly simulate it and to assess its stationarity, given the short satellite observation record. Such quantification may impact assessments of Arctic sea-ice predictability on seasonal-to-interannual timescales.

Indeed, recent work has shown that in a CMIP5 GCM (CESM1-CAM5) the tropics have a modest impact on seasonal forecast skill for Arctic sea ice (e.g., Blanchard-Wrigglesworth & Ding, 2019), which suggests less of a role for tropical teleconnections. Yet, this result is contingent on the GCM correctly simulating teleconnections to the Arctic from the tropics. If a particular GCM does not simulate the correct tropical-polar linkage, remote prediction skill may be underestimated. It has been noted, for instance, that CESM1-CAM5 does not replicate the PARC teleconnection well enough (Baxter et al., 2019). However, it remains unknown whether this is because of model bias or internally-generated variability (Blanchard-Wrigglesworth & Ding, 2019). Likewise, there is growing evidence that teleconnections can shift both in space and time over decadal and centennial timescales (e.g., Coats et al., 2013; Raible et al., 2014; Batehup et al., 2015; Dätwyler et al., 2018; Kolstad & Screen, 2019). But because of the temporally-limited satellite observation record, it is difficult to quantify the stationarity of the PARC teleconnection. These issues raise two important questions that we address in this work: (i) do GCMs simulate the observed PARC teleconnection and (ii) how robust and stationary is the PARC teleconnection?

Using output from 30 CMIP5 models, we evaluate the skill of GCMs in simulating the PARC teleconnection and characterize its stationarity on decadal and centennial timescales. We first discuss the PARC teleconnection between summertime SSTs and September Arctic SIE in the satellite observation record (1979–2018). We then compute this relationship across unforced control simulations in CMIP5 and show that GCMs can simulate the PARC teleconnection over 40-year periods, but not over longer, centennial timescales. Finally, using continuous 40-year segments from the unforced control simulations, we demonstrate that GCMs exhibit considerable PARC teleconnection variability on multidecadal timescales.

2 Data

2.1 Observational datasets

For observation-based data of the geopotential height at 200 hPa (Z200), we use the NCEP-NCAR reanalysis (Kalnay et al., 1996). We choose the Z200 field since this metric characterizes tropospheric circulation patterns associated with sea ice variability (Ding et al., 2017, 2019). For SST data over the observation period, we use the Hadley Centre's sea ice and sea surface temperature (HadISST.2) dataset (Rayner et al., 2003). Note, this analysis is insensitive to the choice of reanalysis dataset (e.g., ERA-Interim). We regrid both fields to a 1.0° $\times$ 1.0° analysis grid using the nearest-neighbor interpolation. Since regridding can result in differences from the original grid (Hofstra et al., 2008), we compare the adjusted and orginal grid and find little difference. Monthly Arctic SIE from 1979 to 2018 was derived using observations of monthly sea-ice concentration (SIC) from the National Snow and Ice Data Center (NSIDC) passive microwave retrievals bootstrap algorithm (Comiso et al., 2017). We also use a reconstruction of monthly Arctic SIE from 1953 (Walsh et al., 2017) to analyze teleconnection stationarity over a longer observation period. We choose to begin with the year 1953 to account for uncertainties and lack of data in the Walsh et al. (2017) dataset. After 1953 the 'US Navy's extensive mapping of ice' and other national meteorological institutes led to regular, year round monitoring of the Arctic.

2.2 CMIP5 output

To analyze teleconnection stationarity over longer time periods, we use monthly output from 30 different GCMs participating in CMIP5 (Taylor et al., 2012). We use the preindustrial control, historical, and RCP8.5 simulations. Since the historical simulations end in 2005, to produce a 1979–2018 "satellite observation period" for CMIP5, we merge the 1979–2005 fields from the historical simulations with the 2006–2018 fields under the RCP8.5 forcing scenario (hereafter referred to as "historical-RCP8.5"). At such short time scales and so early in the 21st century, the uncertainty associated with choice of forcing scenario is negligible (Hawkins & Sutton, 2009). For each experiment, we consider three quantities: SIC, SST, and Z200. The set of GCMs evaluated for all three quantities reflect those that provide the necessary output (see Table S1). All model output is regridded to a common $1^\circ \times 1^\circ$ analysis grid using nearest-neighbor interpolation. With each GCM, we compute monthly Arctic SIE (defined as the area where SIC>15%) over 1979–2018 and the 200-year-long preindustrial control run.

3 The Pacific Ocean teleconnection to Arctic sea ice in observations (1979–2018)

We begin by quantifying the PARC teleconnection in observations (1979–2018) through correlation maps analogous to the teleconnection measure used in Wallace and Gutzler (1981). Figure 1a shows the correlation map between global June, July, and August (JJA) SSTs and September Arctic SIE from 1979 to 2018. Note, both datasets were linearly detrended prior to correlation calculations. Over the satellite observation period, there is a modest, but statistically significant (at the 95% confidence level) positive correlation situated in the subequatorial Pacific and the eastern branch of the Pacific Decadal Oscillation (PDO). Such a relationship suggests that positive summertime SST anomalies in the Pacific

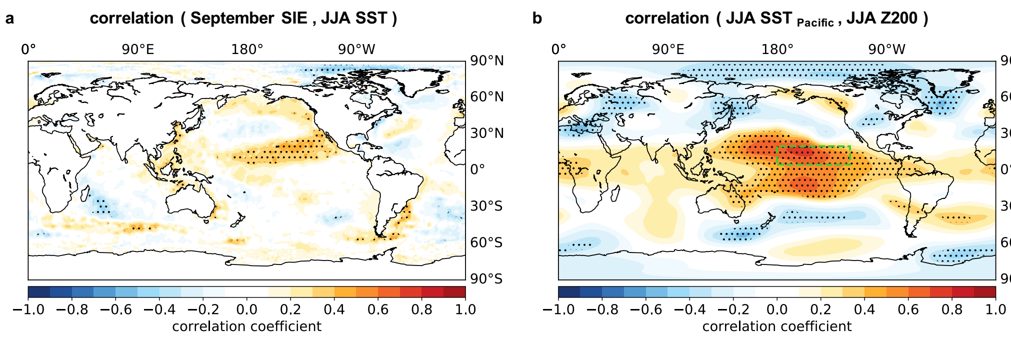

Figure 1. The Pacific Ocean teleconnection to Arctic sea ice in observations (1979–2018). (a) Pearson correlation coefficient between September Arctic sea-ice extent (SIE) and global June, July, and August (JJA) sea surface temperatures (SSTs) from 1979–2018. (b) Pearson correlation coefficient between JJA SST averaged in the dashed green box and global JJA 200 hPa geopotential height (Z200) from 1979–2018. Black dots denote statistically significant correlation coefficient values at the 95% confidence level. All datasets were linearly detrended before correlation coefficient values were calculated.

Ocean are related to positive Arctic SIE anomalies in September. This correlation pattern is similar to the SST pattern that precedes El Niño conditions (Vimont et al., 2003), but the pattern is not related to El Niño itself (we note that in observations September Arctic SIE is uncorrelated with the JJA NINO3.4 index ($r = 0.12$) over 1979–2018). To investigate a causal mechanism, we analyze if there exists an atmospheric bridge linking the two variables. Figure 1b shows the correlation map between JJA SST averaged over the tropical Pacific region that shows highest SST correlations with Arctic SIE (5°N to 20°N and 180° to 120°W, see green dashed box in Fig. 1b) and global JJA Z200 from 1979 to 2018. Again, both datasets were linearly detrended before correlation calculations. Figure 1b shows a statistically significant (at the 95% confidence level) area of negative Z200 correlations throughout the Arctic, with the largest negative correlation coefficient values occurring in the Central Arctic, Canadian Archipelago, Baffin Bay, and Labrador Sea. This correlation suggests that positive SST anomalies in the subequatorial Pacific Ocean generate negative Z200 anomalies throughout the Arctic — which is consistent with cooler tropospheric temperatures and favorable conditions for positive September Arctic SIE anomalies (Ding et al., 2019; Baxter et al., 2019; Olonscheck et al., 2019). This relationship can also be seen through the negative correlation between September Arctic SIE and JJA Z200 throughout the Arctic (see Fig.

S1). This result is also consistent with previous work that has identified similar correlation structures for glacier mass-balance anomalies in the region (e.g., Bonan, Christian, & Christianson, 2019).

4 The Pacific Ocean teleconnection to Arctic sea ice in CMIP5

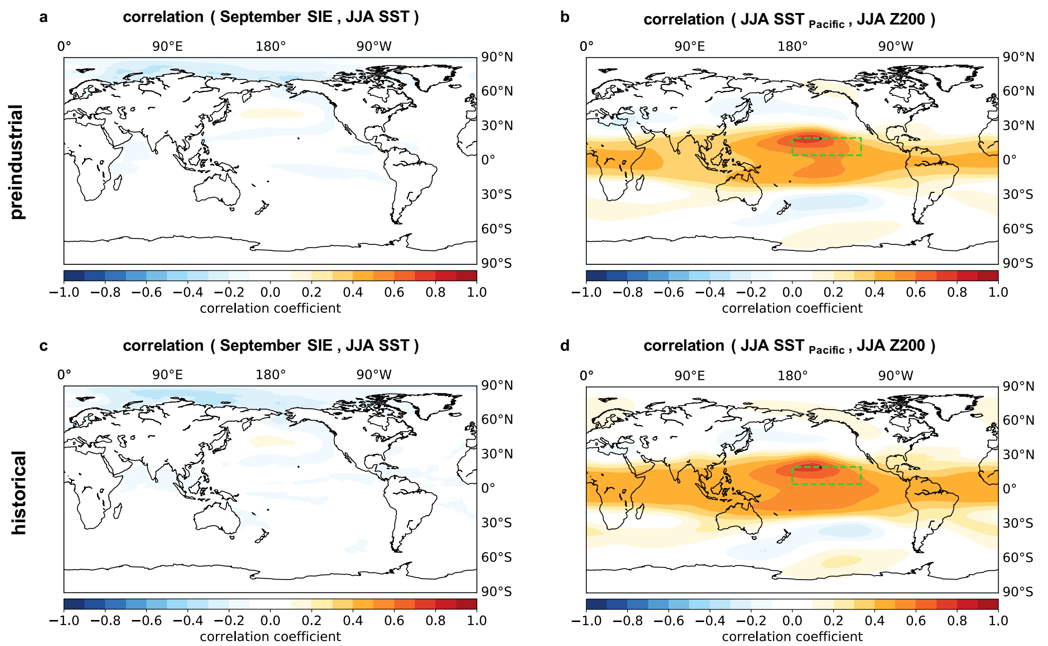

Figure 2. The Pacific Ocean teleconnection to Arctic sea ice in CMIP5. The ensemble mean correlation map between September Arctic sea-ice extent (SIE) and global June, July, and August (JJA) sea surface temperatures (SSTs) across all 30 GCMs using the (a) preindustrial control and (c) historical-RCP8.5 (1979–2018) simulations. The ensemble mean correlation map between JJA SST averaged in the dashed green box and global JJA 200 hPa geopotential height (Z200) across all 30 GCMs using the (b) preindustrial control and (d) historical-RCP8.5 (1979–2018) simulations.

We now turn to output from GCMs participating in CMIP5 by first computing the teleconnection relationship in the preindustrial control simulations. Figure 2a shows the ensemble mean correlation map computed between global JJA SSTs and September Arctic SIE over the 200-year-long preindustrial control run from all 30 GCMs. For each GCM, both datasets were linearly detrended prior to the calculations. Across the entire suite, not a single GCM simulates the observed spatial features in the Pacific Ocean (see Fig. S2). Notably, some of the GCMs (∼11) simulate the opposite relationship, with negative correlations between JJA SSTs and September Arctic SIE in the subequatorial Pacific (see e.g., BCC-CSM1.1(m) in Fig. S2). Additionally, the observed tropical-polar SST-Z200 linkage is not simulated. Figure 2b shows the the ensemble mean correlation map computed between JJA SST averaged over 5°N to 20°N and 180° to 120°W (i.e., the dashed green box) and global JJA Z200 over the 200-year-long preindustrial control run from all 30 GCMs. While GCMs generally agree in showing large positive correlations over the tropical Pacific and a Rossby wave train over the southeastern Pacific Ocean and Southern Ocean, not a single GCM replicates the negative Z200 correlations in the Arctic (see Fig. S3), as seen in the observations (see Fig. 1b). Moreover, GCMs tend to spread the tropical Z200 signal coupled to Pacific SSTs over the whole tropics. Interestingly, BCC-CSM1.1(m), which simulates the strongest SIE-SST relationship opposite to observations (i.e., negative SST correlations in the subequatorial Pacific Ocean), produces a positive correlation between JJA Pacific SST and JJA Z200 in the Arctic (see Fig. S3), which is also opposite to the observed relationship.

The above analysis is computed across 200-year-long unforced control simulations. To investigate if the teleconnection is only present at shorter timescales and under modern day conditions, we compute the PARC teleconnection in the CMIP5 historical-RCP8.5 simulations. Figure 2c shows the ensemble mean correlation map computed between global JJA SSTs and September Arctic SIE over 1979–2018 from all 30 GCMs (after linearly detrending all variables). Despite using a 40-year time period — which is substantially shorter than the 200-year-long preindustrial control run — most GCMs do not accurately simulate the observed teleconnection (see Fig. S4). Similarly, the crucial atmospheric bridge that links the Pacific Ocean to Arctic sea ice is absent. Figure 2d shows the the ensemble mean correlation map computed between JJA SST averaged over 5°N to 20°N and 180° to 120°W (i.e., the green box) and global JJA Z200 over 1979–2018 from all 30 GCMs. GCMs show robust positive correlation values throughout the tropics and a Rossby wave train to the Southern Ocean, but again struggle to simulate a negative relationship in the Arctic. Notably, while the ensemble mean correlation map lacks the statistically-significant negative Z200 correlation structure over the Arctic, CMCC-CMS — which most closely resembles the observed teleconnection pattern (i.e., Fig. 1a) — does indeed simulate the linkage (see Fig. S4 and S5), with negative Z200 correlation values throughout the Arctic. This result lends credence that GCMs may indeed be able to simulate this relationship.

4.1 Multidecadal teleconnection variability

The inability of GCMs to simulate the observed PARC teleconnection suggests that either model bias is impacting the relationship between the Pacific Ocean and Arctic sea ice, or that there is significant internal variability in the evolution of this teleconnection and observations sample an extreme realization. For instance, Blanchard-Wrigglesworth and Ding (2019) note that although the ensemble mean of 40 large ensemble members in CESM1(CAM5) fails to simulate the Pacific Ocean teleconnection to Arctic sea ice, individual ensemble members are able to simulate the correct relationship, which suggests a role for internal variability.

To investigate teleconnection stationarity over longer timescales, the preindustrial control simulations were divided into continuous 40-year segments to match the length of the satellite observation record (1979–2018), generating a set of 160 segments for each control run. For each segment, the correlation map between September Arctic SIE and JJA SSTs was calculated and compared to the observed correlation map (see Fig. 1a), by determining the pattern correlation, ρ, between the two correlation maps. Before the pattern correlation values were determined we restricted the spatial domain of both the observational map (i.e., Fig. 1a) and each map of the 160 segments from 0° to 65°N and 90°E to 90°W since the north Pacific Ocean is the primary region of interest. As noted by Raible et al. (2014), the pattern correlation is a strict skill metric, where even a spatial pattern offset by a two grid points will cause the pattern correlation value, ρ, to deteriorate from $\rho = 1.0$ to approximately $\rho = 0.85$. The range in pattern correlation values is thus interpreted as a measure of the temporal stationarity of the teleconnection for a given GCM.

The pattern correlation values, ρ, for each GCM are shown in Figure 3a. The mean for all GCMs falls below the significance threshold ($\sim$0.31; see grey shading in Fig. 3a), and is thus statistically indistinguishable from a correlation value of 0.0. This result is consistent with the correlation maps from the 200-year-long unforced control simulations, which show little-to-no teleconnection (see Fig. 2a). It also suggests that the PARC teleconnection is often inactive. Notably, the GCMs (e.g., BCC-CSM1.1(m)) with mean negative correlation values ($\bar{\rho} < 0$) are also the GCMs whose 200-year-long correlation map tended toward an opposite relationship to observations (see Fig. S2). Furthermore, some GCMs (e.g., BCC-CSM1.1, BCC-CSM1.1(m), and MIROC5) show less variability in the teleconnectivity, while others (e.g., CCSM4, CESM1(CAM5), and HadGEM2-CC) exhibit a considerable range of

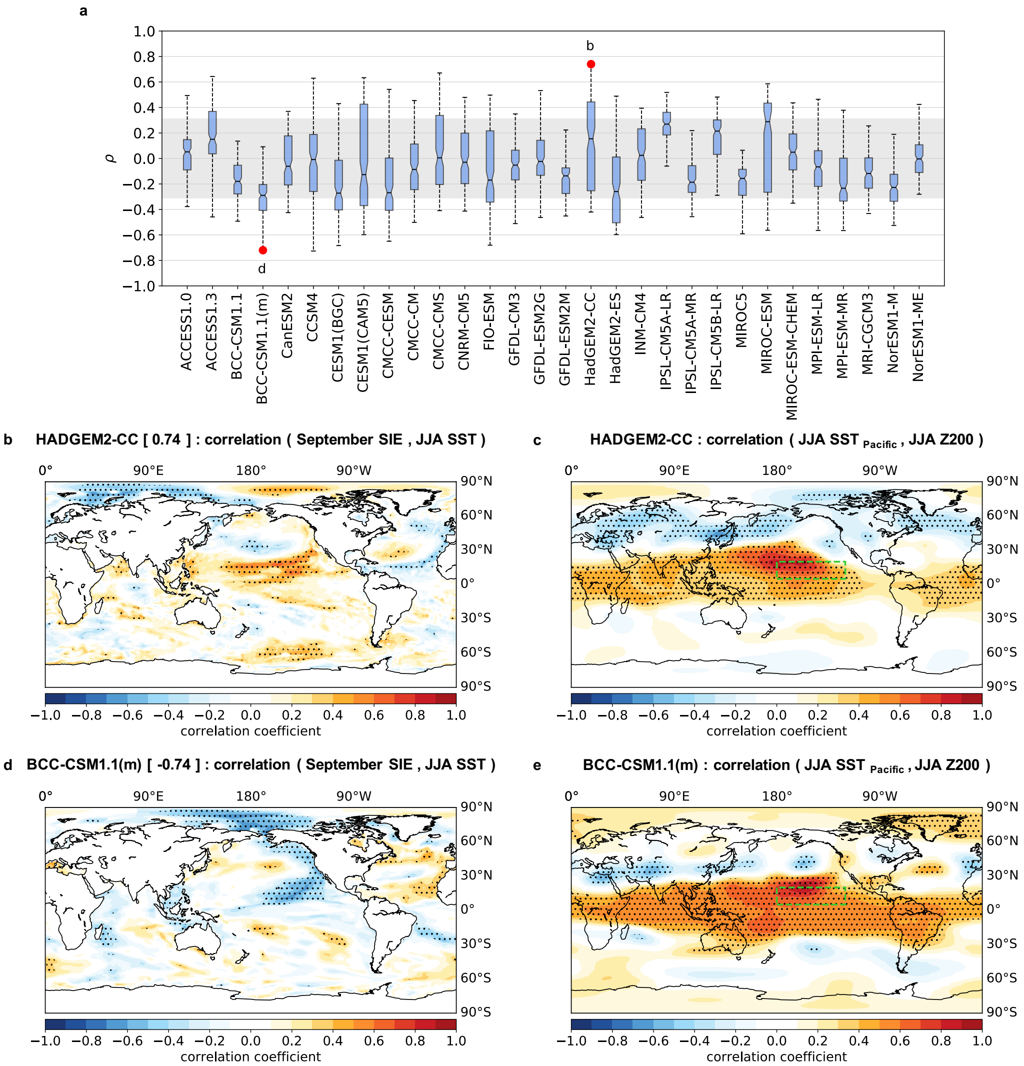

Figure 3. Illustration of variability in the Pacific Ocean teleconnection to Arctic sea ice. (a) Pacific Ocean teleconnection stationarity, as measured by the pattern correlation, ρ, of the North Pacific Ocean (0° to 65°N, 90°E to 90°W), using the Pacific Ocean teleconnection map estimated from observations (Fig. 1a) and continuous 40-year segments from the 200-year-long preindustrial control simulations. Box plots indicate the 25th and 75th percentile of the pattern correlation statistic across the segments in each respective GCM with the mean as the central line and the whiskers showing the full data range. The grey shading represents the bounds of statistically-significant values at the 95% confidence level. The letters denote the correlation map for (b) and (d). The Pacific Ocean teleconnection map from the most positive pattern correlation value (Fig. 3b) and the most negative pattern correlation value (Fig. 3d), respectively, and the corresponding SST-Z200 correlation map (Fig. 3c and Fig. 3e). The bracketed numbers in Fig. 3b and Fig. 3d are the pattern correlation values with the observed teleconnection map.

pattern correlation values. Although such a large inter-model spread exists in the ability of GCMs to simulate this teleconnection, we focus here on the ability of GCMs to simulate the relationship during any given 40-year segment.

Figure 3b shows the correlation map of global JJA SSTs and September Arctic SIE for the GCM with the most positive pattern correlation value (i.e., HadGEM2-CC, $\rho = 0.74$) and Figure 3d shows the correlation map of global JJA SSTs and September Arctic SIE for a GCM with the most negative pattern correlation value (i.e., BCC-CSM1.1(m), $\rho = -0.74$). In Fig. 3b a statistically-significant positive correlation is situated in the subequatorial Pacific Ocean, almost identical to observations. Furthermore, the atmospheric bridge (i.e., the correlation map between JJA Pacific SST and global JJA Z200) shows a statistically-significant (at the 95% confidence level) negative correlation value off the coast of Greenland and over the Canadian Archipelago (see Fig. 3c). Conversely, BCC-CSM1.1(m) shows a statistically-significant (at the 95% confidence level) region of negative correlation in the subequatorial Pacific Ocean (see Fig. 3d). Similarly, the atmospheric bridge, which is the correlation map between JJA Pacific SST and global JJA Z200, shows a statistically-significant positive correlation region over Greenland and the Barents Sea (see Fig. 3e). While this result suggests some GCMs are capable of simulating the teleconnection between the Pacific Ocean and Arctic sea ice, there is significant spread, both in time and across GCMs, in the simulated character of this teleconnection.

4.2 Non-stationary atmospheric bridge

Even within a single GCM, there is considerable variability in the simulated character of the PARC teleconnection over multidecadal timescales. This non-stationarity leads us to ask how stationary is the atmospheric bridge linking the Pacific Ocean to Arctic sea ice? Following from the previous 40-year segment analysis, the set of 160 segments for each control run was used to compute the correlation between JJA Pacific SST (the green box) and global JJA Z200. The correlation maps of each member were then averaged from 70°N to 90°N and 180° to 90°W to capture the SST-Z200 relationship in the Arctic (see y-axis of Fig. 4). Similarly, the SST-SIE correlation maps of each GCM (i.e., Fig. 3) were averaged from 5°N to 20°N and 180° to 90°W to capture the SIE-SST relationship in the Pacific (see x-axis of Fig. 4). The two values from all 160 slices across all 30 GCMs were then compared to evaluate the relationship between strong positive correlations from JJA Pacific SST and

September Arctic SIE (i.e., the PARC teleconnection) and strong negative correlations from JJA Pacific SST and JJA Z200 (i.e., the atmospheric bridge to the Arctic from the Pacific).

Figure 4 shows scatter plots of the relationship described above in each GCM. GCMs tend to show two different behaviors: a cluster of values centered around 0.0 for both the SIE-SST and SST-Z200 correlations, indicating that no PARC teleconnection is simulated (e.g., ACCESS1.3, CMCC-CM) and another cluster of values that show opposite correlation signs during different periods, indicating that a PARC teleconnection is simulated (e.g., CCSM4, HadGEM2-CC). As mentioned above, this means that during some periods, positive SST anomalies in the Pacific Ocean lead to negative Z200 anomalies in the Arctic and positive Arctic SIE anomalies. Interestingly, during other periods these same GCMs simulate an opposite teleconnection to PARC: positive SST anomalies in the Pacific Ocean lead to positive Z200 anomalies in the Arctic and negative Arctic SIE anomalies. This illustrates a non-stationary teleconnection between the Pacific Ocean and Arctic sea ice in GCMs.

Can one assess the stationarity of the PARC teleconnection in observations? To analyze this, we use a reconstruction of September Arctic SIE (Walsh et al., 2017) and HadISST.2 SSTs from 1953 to present. We then divide the record into 40-year segments beginning in 1953. We select 1953 as this is when more extensive sea ice observations become available (Walsh et al., 2017). This produces a set of 26 segments and allows us to examine teleconnection stationarity in observations. We then compute the correlation maps between JJA SST and September Arctic SIE and average over the correlation values from 5°N to 20°N and 180° to 90°W. Likewise, we compute the correlation maps between JJA Pacific SST and JJA Z200 and average over the correlation values from 70°N to 90°N and 180° to 90°W. The light red dots show the range of correlation values in observations, with the large dark red dot showing the relationship calculated over the satellite era (i.e., 1979–2018). Notably, only the GCMs with large non-stationarity in the PARC teleconnection (e.g., CCSM4, HadGEM2-CC, IPSL-CM5A-LR, and NorESM1-ME) are within the range of the satellite era PARC teleconnection (see large red dot). Conversely, some GCMs (e.g., CMCC-CM, HadGEM2-ES, MIROC-ESM, MIROC-ESM-CHEM, MPI-ESM-MR, and MRI-CGCM3) show little-to-no relationship (or the opposite relationship), suggesting that some GCMs are unable to replicate the observed teleconnection linkage. However, this could be due to the choice of averaging region; some GCMs may have a different region of maximal correlation possibly due to model bias. Importantly, it becomes clear that during the earlier parts of the observational record, the PARC teleconnection was not present (note

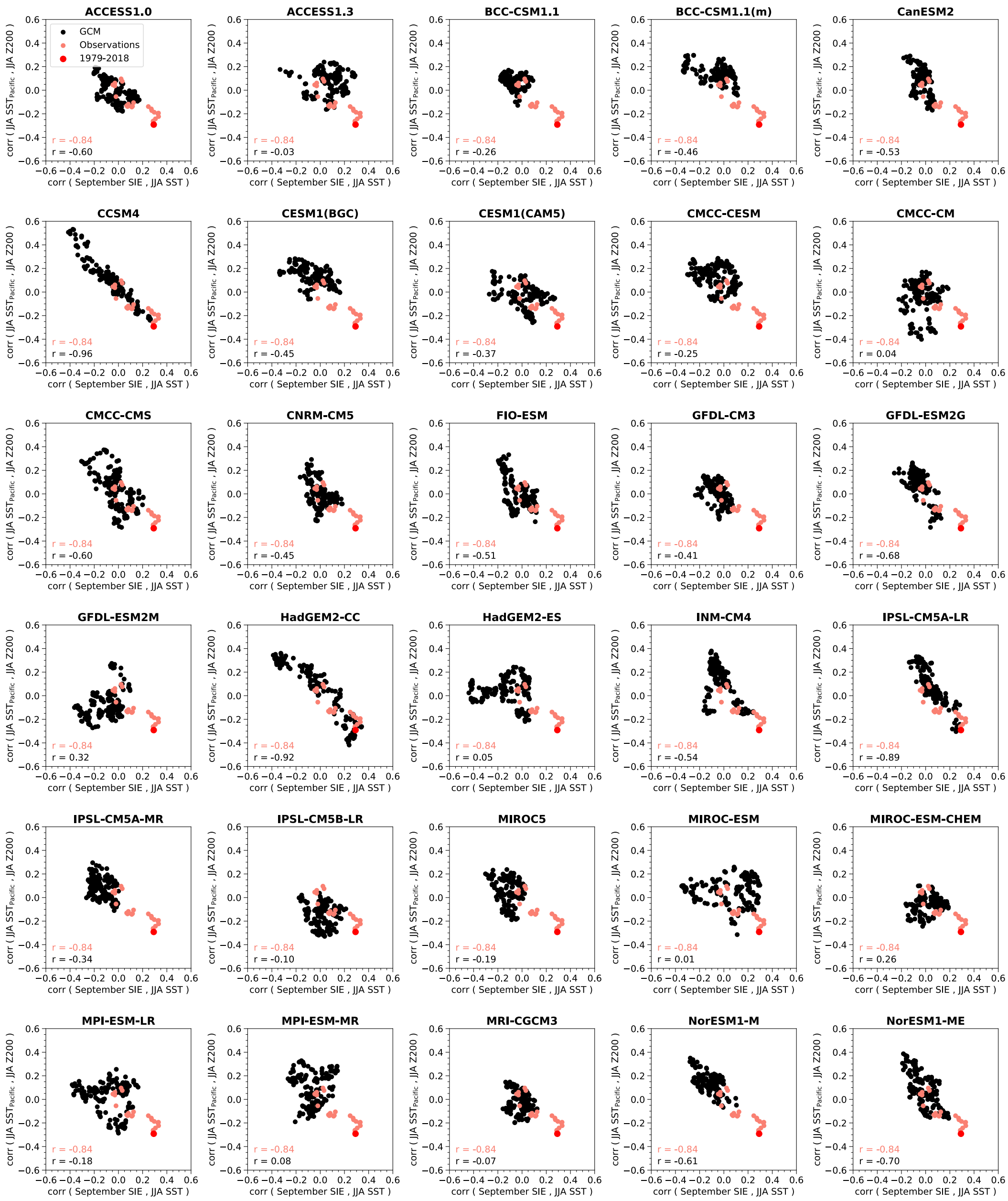

Figure 4. The relationship between the SIE-SST correlation values and SST-Z200 correlation values in each GCM. The x-axis shows the average correlation value over the region that shows highest SIE-SST correlations in the observed teleconnection pattern (5°N to 20°N, 180° to 90°W) using values from each of the continuous 40-year segments of the 200-year-long preindustrial control simulations. The y-axis shows the average correlation value over the region that shows highest SST-Z200 correlations in the observed teleconnection pattern (70°N to 90°N, 180° to 90°W) using values from each of the continuous 40-year segments of the 200-year-long preindustrial control simulations. The correlation between the variables of each GCM is shown in the bottom left corner of each plot. The light red dots show the same relationship using continuous 40-year segments from reanalysis datasets, where the large dark red dot is the observed teleconnection relationship in the satellite record (1979–2018). The correlation using the reanalysis datasets is also shown in the bottom left corner of each plot.

the light red dots clustered around 0.0). Though, we note that uncertainties in the sea ice data between 1953 and the satellite era may impact these results. From 1953 to 1992, there are no statistically significant correlation values in the Pacific Ocean (see Fig. S6). This suggests — as seen in the GCMs that do temporarily simulate the observed teleconnection — the PARC teleconnection is also non-stationary in the real world.

5 Discussion and conclusions

Understanding the processes leading to Arctic sea ice change allows us to better interpret observed changes and better predict future changes. Recent studies have shown that summertime SSTs in the subequatorial Pacific Ocean can affect September Arctic sea ice through atmospheric wave propagation (e.g., Ding et al., 2019; Baxter et al., 2019). Indeed, we find across the observational record (1979–2018) there are statistically significant correlation coefficient values between September Arctic SIE and JJA SSTs in the subequatorial Pacific Ocean (see Fig. 1a). In this region, positive JJA SST anomalies generate negative JJA Z200 anomalies throughout the Arctic (see Fig. 1b), which is consistent with conditions favorable for positive September Arctic SIE anomalies (Ding et al., 2019; Baxter et al., 2019; Olonscheck et al., 2019). Referred to as the "Pacific-Arctic (PARC) teleconnection", this mode is thought to have — in conjunction with anthropogenic climate change — contributed to Arctic sea ice loss in recent years (Baxter et al., 2019). Yet, much of our understanding of this teleconnection is derived from a temporally-limited satellite observation record, which means we may not fully understand how this teleconnection evolves over time. Furthermore, GCMs may be unable to replicate the observed teleconnection (Blanchard-Wrigglesworth & Ding, 2019; Baxter et al., 2019). To address these concerns, we used output from CMIP5 to evaluate the ability of GCMs to simulate this teleconnection and further characterize its stationarity on decadal and centennial timescales.

By investigating this teleconnection across 200-year-long unforced control simulations, we find that GCMs are unable to accurately simulate this teleconnection on centennial timescales (Fig. 2a-b). Even on 40-year timescales that occur during the observed historical period (1979–2018), we find most GCMs are unable to accurately simulate this teleconnection (Fig. 2c-d). However, by splitting the 200-year-long unforced control simulations into continuous 40-year segments that match the length of the observational record, we show that a minority of GCMs are able to temporarily simulate the observed teleconnection, but these GCMs exhibit considerable variability on multidecadal timescales (see Fig. 3a). In these GCMs, positive JJA SST anomalies in the subequatorial Pacific Ocean generate negative JJA Z200 anomalies throughout the Arctic (Fig. 3b-c), but during other times the reverse relationship is simulated, as positive JJA SST anomalies in the subequatorial Pacific Ocean generate positive JJA Z200 anomalies throughout the Arctic (Fig. 3d-e). Since Z200 anomalies affect tropospheric temperatures in the Arctic (Ding et al., 2017, 2019; Baxter et al., 2019), these Pacific Ocean SST anomalies modulate Arctic sea ice loss. A potential caveat to this assessment is the significant spread in the ability of GCMs to correctly simulate the PARC teleconnection. These inter-model differences could be due to model biases in SST variability in the subequatorial Pacific Ocean. For instance, a GCM with weak SST variability in this region is likely to have insufficient variability in convection and Rossby wave generation and hence a weaker teleconnection. Indeed, we find that GCMs with lower pattern correlation values tend to have weaker Pacific SST variability, but the variability is still within range of observations (see Fig. S7). Another possible model bias could be the response of the tropical atmosphere to diabatic heating in the subequatorial Pacific Ocean. While GCMs are able to capture the relationship between September Arctic SIE and JJA Z200 in the Arctic (see Fig. S1), the tropical Z200 signal associated with the subtropical Pacific SST anomaly spreads too zonally when compared to observations. While it is beyond the scope of this paper to diagnose this feature further, we note that subtle changes in the source region of planetary waves can strongly influence their path and thus associated teleconnections at higher latitudes (e.g., Hoskins & Karoly, 1981). Such a discrepancy suggests that GCMs may be unable to capture the critical first step of the PARC teleconnection and could explain why the PARC teleconnection is absent in many GCMs. Further characterizations of inter-model differences may improve our understanding of the PARC teleconnection behavior and elucidate the role of model biases versus internal variability.

Our analysis suggests substantial variability in the simulated character of this teleconnection, with an equally non-stationary atmospheric bridge from the subequatorial Pacific Ocean to the Arctic (see Fig. 4). Although this teleconnection is often dormant, large decadal variability can give rise to rare multidecadal periods where the PARC teleconnection is active, like that seen during 1979–2018. Additionally, as evinced by the PARC teleconnection not being present in the earlier part of the observational record (1953–1992), it is plausible that the observed relationship between the Pacific Ocean and Arctic sea ice will change in the coming decades. Even on shorter timescales, there is a stark contrast in the relationship between September Arctic SIE and summertime SSTs in the Pacific Ocean. During 1979–1998, no PARC teleconnection is present, whereas during 1999–2018 there is a clear connection to a pattern reminiscent of the PDO (see Fig. S8). Given such clear non-stationarity, we caution use of statistical reconstructions and predictions of Arctic sea ice using Pacific SST information. Statistical models rely almost exclusively on fixed relationships between Arctic sea ice and predictor variables, implying that the processes affecting Arctic sea ice do not change over time. On the other hand, because dynamical models can simulate this relationship, GCMs may be useful tools to study the processes that give rise to non-stationarity. Better understanding the origins of this non-stationarity will improve predictions and projections of Arctic sea ice, possibly helping to inform us when the Arctic will be ice free.

Acknowledgments

This work benefited from insightful discussions with C.M. Bitz and J.M. Wallace. The authors are grateful for helpful comments from D.S. Battisti and F. Lehner and thank L.A. Parsons for a detailed review on a draft of this manuscript. The authors also thank the climate modeling groups for producing and making available their model output, which is accessible at the Earth System Grid Federation (ESGF) Portal (https://esgf-node.llnl.gov/search/cmip5/). E.B.W. was supported by NOAA MAPP Grant NA18OAR4310274.

References

Batehup, R., McGregor, S., & Gallant, A. (2015). The influence of non-stationary teleconnections on palaeoclimate reconstructions of ENSO variance using a pseudoproxy framework. *Climate of the Past*, *11*(12), 1733–1749.

Baxter, I., Ding, Q., Schweiger, A., LHeureux, M., Baxter, S., Wang, T., … Lu, J. (2019). How tropical Pacific surface cooling contributed to accelerated sea ice melt from 2007 to 2012 as ice is thinned by anthropogenic forcing. *Journal of Climate*, *0*(0), null. doi: 10.1175/JCLI-D-18-0783.1

Blanchard-Wrigglesworth, E., Armour, K. C., Bitz, C. M., & DeWeaver, E. (2011). Persistence and inherent predictability of Arctic sea ice in a GCM ensemble and observations. *Journal of Climate*, *24*(1), 231–250.

Blanchard-Wrigglesworth, E., Bitz, C., & Holland, M. (2011). Influence of initial conditions and climate forcing on predicting Arctic sea ice. *Geophysical Research Letters*, *38*(18).

Blanchard-Wrigglesworth, E., & Bushuk, M. (2019). Robustness of Arctic sea-ice predictability in GCMs. *Climate Dynamics*, *52*(9-10), 5555–5566.

Blanchard-Wrigglesworth, E., Cullather, R., Wang, W., Zhang, J., & Bitz, C. (2015). Model forecast skill and sensitivity to initial conditions in the seasonal Sea Ice Outlook. *Geophysical Research Letters*, *42*(19), 8042–8048.

Blanchard-Wrigglesworth, E., & Ding, Q. (2019). Tropical and midlatitude impact on seasonal polar predictability in the Community Earth System Model. *Journal of Climate*, *32*(18), 5997–6014.

Bonan, D. B., Bushuk, M., & Winton, M. (2019). A spring barrier for regional predictions of summer Arctic sea ice. *Geophysical Research Letters*, *46*(8), 5131–5140.

Bonan, D. B., Christian, J. E., & Christianson, K. (2019). Influence of North Atlantic climate variability on glacier mass balance in Norway, Sweden and Svalbard. *Journal of Glaciology*, *65*(252), 580–594.

Bushuk, M., Msadek, R., Winton, M., Vecchi, G., Yang, X., Rosati, A., & Gudgel, R. (2019). Regional Arctic sea–ice prediction: potential versus operational seasonal forecast skill. *Climate Dynamics*, *52*(5-6), 2721–2743.

Bushuk, M., Msadek, R., Winton, M., Vecchi, G. A., Gudgel, R., Rosati, A., & Yang, X. (2017). Skillful regional prediction of Arctic sea ice on seasonal timescales. *Geophysical Research Letters*, *44*(10), 4953–4964.

Castruccio, F. S., Ruprich-Robert, Y., Yeager, S. G., Danabasoglu, G., Msadek, R., & Delworth, T. L. (2019). Modulation of Arctic sea ece loss by atmospheric teleconnections from Atlantic multidecadal variability. *Journal of Climate*, *32*(5), 1419–1441.

Chevallier, M., Salas y Mélia, D., Voldoire, A., Déqué, M., & Garric, G. (2013). Seasonal forecasts of the pan-Arctic sea ice extent using a GCM-based seasonal prediction system. *Journal of Climate*, *26*(16), 6092–6104.

Coats, S., Smerdon, J. E., Cook, B. I., & Seager, R. (2013). Stationarity of the tropical pacific teleconnection to North America in CMIP5/PMIP3 model simulations. *Geophysical Research Letters*, *40*(18), 4927–4932.

Comiso, J. C., Meier, W. N., & Gersten, R. (2017). Variability and trends in the Arctic sea ice cover: Results from different techniques. *Journal of Geophysical Research: Oceans*, *122*(8), 6883–6900.

Comiso, J. C., Parkinson, C. L., Gersten, R., & Stock, L. (2008). Accelerated decline in the Arctic sea ice cover. *Geophysical research letters*, *35*(1).

Dätwyler, C., Neukom, R., Abram, N. J., Gallant, A. J., Grosjean, M., Jacques-Coper, M., ... Villalba, R. (2018). Teleconnection stationarity, variability and trends of the Southern Annular Mode (SAM) during the last millennium. *Climate dynamics*, *51*(5-6), 2321–2339.

Day, J., Hawkins, E., & Tietsche, S. (2014). Will Arctic sea ice thickness initialization improve seasonal forecast skill? *Geophysical Research Letters*, *41*(21), 7566–7575.

Day, J., Tietsche, S., & Hawkins, E. (2014). Pan-Arctic and regional sea ice predictability: Initialization month dependence. *Journal of Climate*, *27*(12), 4371–4390.

Ding, Q., Schweiger, A., LHeureux, M., Battisti, D. S., Po-Chedley, S., Johnson, N. C., ... others (2017). Influence of high-latitude atmospheric circulation changes on summertime Arctic sea ice. *Nature Climate Change*, *7*(4), 289.

Ding, Q., Schweiger, A., LHeureux, M., Steig, E. J., Battisti, D. S., Johnson, N. C., ... others (2019). Fingerprints of internal drivers of Arctic sea ice loss in observations and model simulations. *Nature Geoscience*, *12*(1), 28.

Ding, Q., Wallace, J. M., Battisti, D. S., Steig, E. J., Gallant, A. J., Kim, H.-J., & Geng, L. (2014). Tropical forcing of the recent rapid Arctic warming in northeastern Canada and Greenland. *Nature*, *509*(7499), 209.

Dirkson, A., Merryfield, W. J., & Monahan, A. (2017). Impacts of sea ice thickness initialization on seasonal Arctic sea ice predictions. *Journal of Climate*, *30*(3), 1001–1017.

Eicken, H. (2013). Ocean science: Arctic sea ice needs better forecasts. *Nature*, *497*(7450), 431.

Ford, J. D., & Smit, B. (2004). A framework for assessing the vulnerability of communities in the Canadian Arctic to risks associated with climate change. *Arctic*, *57*(4), 389–400.

Guemas, V., Blanchard-Wrigglesworth, E., Chevallier, M., Day, J. J., Déqué, M., Doblas-Reyes, F. J., ... others (2016). A review on Arctic sea-ice predictability and prediction on seasonal to decadal time-scales. *Quarterly Journal of the Royal Meteorological Society*, *142*(695), 546–561.

Hawkins, E., & Sutton, R. (2009). The potential to narrow uncertainty in regional climate predictions. *Bulletin of the American Meteorological Society*, *90*(8), 1095–1108.

Hofstra, N., Haylock, M., New, M., Jones, P., & Frei, C. (2008). Comparison of six methods for the interpolation of daily, European climate data. *Journal of Geophysical Research: Atmospheres*, *113*(D21).

Holland, M. M., Bailey, D. A., & Vavrus, S. (2011). Inherent sea ice predictability in the rapidly changing Arctic environment of the Community Climate System Model, version 3. *Climate dynamics*, *36*(7-8), 1239–1253.

Hoskins, B. J., & Karoly, D. J. (1981). The steady linear response of a spherical atmosphere to thermal and orographic forcing. *Journal of the Atmospheric Sciences*, *38*(6), 1179–1196.

Hu, C., Yang, S., Wu, Q., Li, Z., Chen, J., Deng, K., ... Zhang, C. (2016). Shifting El Niño inhibits summer Arctic warming and Arctic sea-ice melting over the Canada Basin. *Nature communications*, *7*, 11721.

Johannessen, O. M., Shalina, E. V., & Miles, M. W. (1999). Satellite evidence for an Arctic sea ice cover in transformation. *Science*, *286*(5446), 1937–1939.

Jung, T., Gordon, N. D., Bauer, P., Bromwich, D. H., Chevallier, M., Day, J. J., ... others (2016). Advancing polar prediction capabilities on daily to seasonal time scales. *Bulletin of the American Meteorological Society*, *97*(9), 1631–1647.

Kalnay, E., Kanamitsu, M., Kistler, R., Collins, W., Deaven, D., Gandin, L., ... others (1996). The NCEP/NCAR 40-year reanalysis project. *Bulletin of the American meteorological Society*, *77*(3), 437–472.

Kapsch, M.-L., Graversen, R. G., & Tjernström, M. (2013). Springtime atmospheric energy transport and the control of Arctic summer sea-ice extent. *Nature Climate Change*, *3*(8), 744.

Kay, J. E., Holland, M. M., & Jahn, A. (2011). Inter-annual to multi-decadal Arctic sea ice extent trends in a warming world. *Geophysical Research Letters*, *38*(15).

Kolstad, E., & Screen, J. (2019). Non-stationary relationship between autumn Arctic sea ice and the winter North Atlantic Oscillation. *Geophysical Research Letters*.

Kwok, R., & Rothrock, D. (2009). Decline in Arctic sea ice thickness from submarine and ICESat records: 1958–2008. *Geophysical Research Letters*, *36*(15).

L'Heureux, M. L., Kumar, A., Bell, G. D., Halpert, M. S., & Higgins, R. W. (2008). Role of the Pacific-North American (PNA) pattern in the 2007 Arctic sea ice decline. *Geophysical Research Letters*, *35*(20).

Maslanik, J., Stroeve, J., Fowler, C., & Emery, W. (2011). Distribution and trends in Arctic sea ice age through spring 2011. *Geophysical Research Letters*, *38*(13).

Meehl, G. A., Chung, C. T., Arblaster, J. M., Holland, M. M., & Bitz, C. M. (2018). Tropical decadal variability and the rate of Arctic sea ice decrease. *Geophysical Research Letters*, *45*(20), 11–326.

Melia, N., Haines, K., & Hawkins, E. (2016). Sea ice decline and 21st century trans-Arctic shipping routes. *Geophysical Research Letters*, *43*(18), 9720–9728.

Merryfield, W., Lee, W.-S., Wang, W., Chen, M., & Kumar, A. (2013). Multi-system seasonal predictions of Arctic sea ice. *Geophysical Research Letters*, *40*(8), 1551–1556.

Msadek, R., Vecchi, G., Winton, M., & Gudgel, R. (2014). Importance of initial conditions in seasonal predictions of Arctic sea ice extent. *Geophysical Research Letters*, *41*(14), 5208–5215.

Ogi, M., Yamazaki, K., & Wallace, J. M. (2010). Influence of winter and summer surface wind anomalies on summer Arctic sea ice extent. *Geophysical Research Letters*, *37*(7).

Olonscheck, D., Mauritsen, T., & Notz, D. (2019). Arctic sea-ice variability is primarily driven by atmospheric temperature fluctuations. *Nature Geoscience*, *12*(6), 430.

Petty, A., Schröder, D., Stroeve, J., Markus, T., Miller, J., Kurtz, N., … Flocco, D. (2017). Skillful spring forecasts of September Arctic sea ice extent using passive microwave sea ice observations. *Earth's Future*, *5*(2), 254–263.

Pizzolato, L., Howell, S. E., Dawson, J., Laliberté, F., & Copland, L. (2016). The influence of declining sea ice on shipping activity in the Canadian Arctic. *Geophysical Research Letters*, *43*(23), 12–146.

Raible, C., Lehner, F., González-Rouco, J., & Fernández-Donado, L. (2014). Changing correlation structures of the Northern Hemisphere atmospheric circulation from 1000 to 2100 AD. *Climate of the Past*, *10*(2), 537–550.

Rayner, N., Parker, D. E., Horton, E., Folland, C. K., Alexander, L. V., Rowell, D., … Kaplan, A. (2003). Global analyses of sea surface temperature, sea ice, and night marine air temperature since the late nineteenth century. *Journal of Geophysical Research: Atmospheres*, *108*(D14).

Rigor, I. G., & Wallace, J. M. (2004). Variations in the age of Arctic sea-ice and summer sea-ice extent. *Geophysical Research Letters*, *31*(9).

Rothrock, D. A., Yu, Y., & Maykut, G. A. (1999). Thinning of the Arctic sea-ice cover. *Geophysical Research Letters*, *26*(23), 3469–3472.

Schröder, D., Feltham, D. L., Flocco, D., & Tsamados, M. (2014). September Arctic sea-ice minimum predicted by spring melt-pond fraction. *Nature Climate Change*, *4*(5), 353.

Screen, J. A., & Deser, C. (2019). Pacific Ocean variability influences the time of emergence of a seasonally ice-free Arctic Ocean. *Geophysical Research Letters*, *46*(4), 2222–2231.

Screen, J. A., & Francis, J. A. (2016). Contribution of sea-ice loss to Arctic amplification is regulated by Pacific Ocean decadal variability. *Nature Climate Change*, *6*(9), 856.

Serreze, M. C., Holland, M. M., & Stroeve, J. (2007). Perspectives on the Arctic's shrinking sea-ice cover. *science*, *315*(5818), 1533–1536.

Serreze, M. C., & Meier, W. N. (2018). The Arctic's sea ice cover: trends, variability, predictability, and comparisons to the Antarctic. *Annals of the New York Academy of Sciences*.

Sigmond, M., Fyfe, J., Flato, G., Kharin, V., & Merryfield, W. (2013). Seasonal forecast skill of Arctic sea ice area in a dynamical forecast system. *Geophysical Research Letters*, *40*(3), 529–534.

Smith, K. L., Polvani, L. M., & Tremblay, L. B. (2018). The impact of stratospheric circulation extremes on minimum Arctic sea ice extent. *Journal of Climate*, *31*(18), 7169–7183.

Stroeve, J., Holland, M. M., Meier, W., Scambos, T., & Serreze, M. (2007). Arctic sea ice decline: Faster than forecast. *Geophysical research letters*, *34*(9).

Taylor, K. E., Stouffer, R. J., & Meehl, G. A. (2012). An overview of CMIP5 and the experiment design. *Bulletin of the American Meteorological Society*, *93*(4), 485–498.

Tietsche, S., Day, J., Guemas, V., Hurlin, W., Keeley, S., Matei, D., ... Hawkins, E. (2014). Seasonal to interannual Arctic sea ice predictability in current global climate models. *Geophysical Research Letters*, *41*(3), 1035–1043.

Trenberth, K. E., Branstator, G. W., Karoly, D., Kumar, A., Lau, N.-C., & Ropelewski, C. (1998). Progress during TOGA in understanding and modeling global teleconnections associated with tropical sea surface temperatures. *Journal of Geophysical Research: Oceans*, *103*(C7), 14291–14324.

Vimont, D. J., Wallace, J. M., & Battisti, D. S. (2003). The seasonal footprinting mechanism in the pacific: Implications for enso. *Journal of Climate*, *16*(16), 2668–2675.

Wallace, J. M., & Gutzler, D. S. (1981). Teleconnections in the geopotential height field during the Northern Hemisphere winter. *Monthly Weather Review*, *109*(4), 784–812.

Walsh, J. E., Fetterer, F., Scott Stewart, J., & Chapman, W. L. (2017). A database for depicting Arctic sea ice variations back to 1850. *Geographical Review*, *107*(1), 89–107.

Wang, L., Yuan, X., Ting, M., & Li, C. (2016). Predicting summer Arctic sea ice concentration intraseasonal variability using a vector autoregressive model. *Journal of Climate*, *29*(4), 1529–1543.

Wang, W., Chen, M., & Kumar, A. (2013). Seasonal prediction of Arctic sea ice extent from a coupled dynamical forecast system. *Monthly Weather Review*, *141*(4), 1375–1394.

Williams, J., Tremblay, B., Newton, R., & Allard, R. (2016). Dynamic preconditioning of the minimum September sea-ice extent. *Journal of Climate*, *29*(16), 5879–5891.

Woodgate, R. A., Weingartner, T., & Lindsay, R. (2010). The 2007 Bering Strait oceanic heat flux and anomalous Arctic sea-ice retreat. *Geophysical Research Letters*, *37*(1).

Wyllie-Echeverria, T., & Wooster, W. S. (1998). Year-to-year variations in Bering Sea ice cover and some consequences for fish distributions. *Fisheries Oceanography*, *7*(2), 159–170.

Yeager, S. G., Karspeck, A. R., & Danabasoglu, G. (2015). Predicted slowdown in the rate of Atlantic sea ice loss. *Geophysical Research Letters*, *42*(24), 10–704.